Applied Biochemistry and Biotechnology (2023) 195:6959–6978
https://doi.org/10.1007/s12010-023-04466-1

ORIGINAL ARTICLE

Pharmacotherapeutic Potential of Natural Products to Target the SARS-CoV-2 PLpro Using Molecular Screening and Simulation Approaches

Abrar Mohammad Sayaf[1] · Hassaan Ahmad[2] · Muhammad Ammar Aslam[2] · Sidra Abdul Ghani[3] · Saira Bano[3] · Qudsia Yousafi[4] · Muhammad Suleman[5] · Abbas Khan[6,7] · Kar Kheng Yeoh[1] · Dong-Qing Wei[6,7,8,9]

Accepted: 16 March 2023 / Published online: 24 March 2023

Abstract

Because of the essential role of PLpro in the regulation of replication and dysregulation of the host immune sensing, it is considered a therapeutic target for novel drug development. To reduce the risk of immune evasion and vaccine effectiveness, small molecular therapeutics are the best complementary approach. Hence, we used a structure-based drug-designing approach to identify potential small molecular inhibitors for PLpro of SARS-CoV-2. Initial scoring and re-scoring of the best hits revealed that three compounds NPC320891 (2,2-Dihydroxyindene-1,3-Dione), NPC474594 (Isonarciclasine), and NPC474595 (7-Deoxyisonarciclasine) exhibit higher docking scores than the control GRL0617. Investigation of the binding modes revealed that alongside the essential contacts, i.e., Asp164, Glu167, Tyr264, and Gln269, these molecules also target Lys157 and Tyr268 residues in the active site. Moreover, molecular simulation demonstrated that the reported top hits also possess stable dynamics and structural packing. Furthermore, the residues' flexibility revealed that all the complexes demonstrated higher flexibility in the regions 120–140, 160–180, and 205–215. The 120–140 and 160–180 lie in the finger region of PLpro, which may open/close during the simulation to cover the active site and push the ligand inside. In addition, the total binding free energy was reported to be -32.65 ± 0.17 kcal/mol for the GRL0617-PLpro, for the NPC320891-PLpro complex, the TBE was -35.58 ± 0.14 kcal/mol, for the NPC474594-PLpro, the TBE was -43.72 ± 0.22 kcal/mol, while for NPC474595-PLpro complex, the TBE was calculated to be -41.61 ± 0.20 kcal/mol, respectively. Clustering of the protein's motion and FEL further revealed that in NPC474594 and NPC474595 complexes, the drug was seen to have moved inside the binding cavity along with the loop in the palm region harboring the catalytic triad, thus justifying the higher binding of these two molecules particularly. In conclusion, the overall results reflect favorable binding of the identified hits strongly than the control drug, thus demanding in vitro and in vivo validation for clinical purposes.

Keywords SARS-CoV-2 variants · PLpro · Drugs · Free energy · Conformational dynamics

Extended author information available on the last page of the article

Introduction

The coronavirus disease 2019 caused by SARS-CoV-2 (server acute respiratory syndrome CoV-2) was first reported in December 2019 in Wuhan, China, which is causing pneumonia in humans [1]. The exponential rate of inter-human transmission of SARS-CoV-2, which is also called 2019-nCoV or 2019 novel coronavirus, enabled it to spread globally [2]. SARS-CoV-2 wreaked havoc on human health throughout the world owing to upper respiratory complications that result in severe pneumonia and bronchiolitis. Hence, COVID-19 was designated a worldwide pandemic by the World Health Organization (WHO) on March 11, 2020 [3].

SARS-CoV-2, like other coronaviruses, attaches to ACE2 and infects the host cell using the same S protein [4]. The S1 subunit, which consists of CTD and NTD domains, aids virus attachment; however, the integration of viral membrane at the CTD terminus facilitates the S2 subunit. The cleavage of the S1 and S2 subunits yields a basic amino acid-rich furin cleavage site, which is called S2′ [5]. The existence of the S2′ site makes the SARS-CoV-2 unique from others, which activates the fusion of viral and human membranes by adopting irreversible conformations, executing the diffusion of the SARS-CoV-2 into the target cells [6].

After the entry of the virus to the target cells, the translation of ORF1 and ORF1ab is stimulated and produces the two polyproteins (pp1a and pp1ab), which are processed by the PLpro (papain-like protease) and 3CLpro, also called Mpro (main protease) [7]. The main purpose of the aforementioned process is to release 16 non-structural proteins (nsps1-16) which are responsible for the formation of replicase complex and processing of viral genome replication. PLpro releases the nsp1-3 from the polyprotein of the virus, which is essential for the replication of the virus. PLpro's deubiquitinating and deISGylating effects have also been demonstrated to suppress the host's innate immunological response to viral infection [8, 9]. Therefore, in the case of both SARS-CoV and SARS-CoV-2, the PLpro was declared a therapeutic target for the suppression of viral replication [10].

The COVID-19 outbreak has posed serious socioeconomic problems for humanity. The COVID-19 pandemic was not properly controlled by the already authorized antivirals, and we are just now discovering how important it is to develop new antiviral treatments in advance to control the potential outbreaks of this and other zoonotic viruses. One key step in ending the epidemic was faster approval and distribution of the first vaccines. However, there are concerns about the protracted consequences of COVID-19 immune protection in a population with highly diverse seroprevalence in Manaus, Brazil, as well as compelling research that those who have been infected with the Alpha, Beta, and Gamma variants are more vulnerable to the highly infectious Delta variant [11].

For instance, natural products are the best choice to be used against SARS-CoV-2 as they have been used as a remedy for many diseases for centuries. Resveratrol and polyphenols such as hesperetin, hesperidin, and tangeretin from *Curcuma* sp. and *Citrus* sp. are previously reported to target the S protein of SARS-CoV-2. Moreover, natural products including terpenoids, diarylheptanoids, coumarins, and flavonoids are among the potential inhibitors of the SARS-CoV 3CLpro. Using in silico and in vitro approaches, quercetin, gallocatechin gallate, and epigallocatechin gallate have been reported to inhibit the Mpro of SARS-CoV-2. Kaempferol which belongs to flavonoid inhibited the SARS-CoV-2 main protease using in silico and in vitro setup [12–14]. Antiviral agents that complement vaccination are urgently needed to end the COVID-19 pandemic. The SARS-CoV-2 proteome is comprised of essential proteins; however, PLpro is one of the two essential cysteine

proteases, which helps the virus to regulate the process of replication and dysregulates the host immune sensing upon the interaction and deubiquitination of host protein substrates. PLpro exhibits a "thumb–palm–fingers" (multi-domains) organization that works in coordination to perform the essential processes. It also processes the viral polyproteins, targets the host interferon, and NF-κB pathways, and generates a functional replicase complex [15, 16]. Moreover, in SARS-CoV-2 infection models, inhibition of the PLpro protease with small molecules notably lowers the viral loads, indicating that PLpro is a prime candidate for next-generation antiviral development [17]. Because of its essential role in viral replication and immune evasion, PLpro is a promising therapeutic target. Hence, here we perform structure-based virtual screening of the NPASS (natural product activity and species source database) of the SARS-CoV-2 PLpro to identify potential inhibitors from natural sources that could act as promising hits for the treatment of COVID-19. The potential hits were compared with the control drug using molecular simulation and free energy calculation methods. The binding of the best candidates was further validated using post-simulation approaches. The identified hits reported the best activity against PLpro thus demanding further in vitro and in vivo validations.

Materials and Methods

Data Retrieval and Preparation

In the crystal structure of PLpro, a cysteine protease from SARS-CoV-2, the protein was retrieved from the RCSB (PDB ID: 7CJM). The Galaxy Refine online server was used for the energy minimization and refinements of PLpro protein structure [18]. The natural compounds' database NPASS (natural product activity and species source database) was retrieved from http://bidd.group/NPASS/ and filtered for Lipinski's rule of five to remove compounds that do not obey the R5' rule. For this purpose, FAFdrug4 online webserver was used which also corrected the protonated states of each compound.

Molecular Screening of NPASS Database

After preparation, all the retrieved structures were screened against the previously identified active site residues of PLpro protein which mainly involve Asp164, Tyr264, Tyr268, and Gln269 [19]. Therefore, these residues were selected for targeting with the natural compounds. The grid size was set as $48 \times 48 \times 40$, while the grid dimensions were set as 2.603, 36.146, and − 23.347 (x, y, z). EasyDock Vina 2.0 was used for the initial screening of the pre-filtered compounds. Based on high scores, the best hits were processed for the re-docking and rescoring.

Induced Fit Docking (IFD) of the Top Hits

In the next phase, to confirm the final hits, the high-score shortlisted compounds were screened by induced fit docking (IFD) by using the 64 exhaustiveness. The AutoDockFR which uses the AutoDock4 scoring function and enhanced the success rate of docking was used for the induced fit docking [20]. In cross-validation docking, AutoDockFR achieved greater accuracy as well as a considerably faster docking speed than AutoDock Vina [20].

Molecular Dynamics Simulation of the Top Hits

The Amber18 package was used to perform the molecular dynamics simulation of the shortlisted top hits docking complexes [21]. For the complex simulation, the amber GAFF (general force field) and ff19SB force field were applied; however, the antechamber module was used for the drug topologies. Following that, each system was solvated and neutralized using an OPC box of water and Na + counter ions. After that, the two-stage energy-minimization system was used, followed by heating and equilibration. Long-range electrostatic interactions were quantified using the Particle Mesh Ewald (PME) method [22]. For Van der Waals contacts and short-range Columbic interactions, a cut-off value of 1.4 nm was used. A Langevin thermostat was used to keep the temperature constant at 300 K, while a Berendsen barostat was utilized for pressure control. Each complex was simulated with a time step of 2 fs and a total simulation length of 200 ns. CPPTRAJ and PTRAJ were used to assess the dynamics, stability, and other properties of the ligand–protein complexes [23]. Post-simulation analyses were performed using the following equations.

$$RMSD = \sqrt{\frac{\sum d^2 i = 1}{N_{atoms}}} \tag{1}$$

where d_i is the position difference between atoms and i is the reference and superimposed structure. The residues' flexibility was indexed by estimating the root mean square fluctuation (RMSF) employing B-factor [33], which is the most imperative constraint for calculating the flexibility of all residues in a protein. Numerically, the flexibility can be calculated with the given equation:

$$Thermal\ factoror\ B - factor = [(8\pi\ **\ 2)/3](msf) \tag{2}$$

The radius of gyration (Rg) measures the overall size of the protein during simulations. For the calculation of the radius of gyration, the following equation was used.

$$Rg = \sqrt{\frac{\sum_{i=1}^{N} m_i r_i^2}{\sum_{i=1}^{N} m_i}} \tag{3}$$

where *mi* is the mass of the atom *i* and *ri* is the distance of atom *i*.

The Binding Free Energy Calculations

The binding free energy (TBE) for each protein–ligand complex was calculated by using the MMPBSA.PY script considering 2500 snapshots using the following equation [24–27]. This method of calculating free energy is extensively used to estimate the TBE of various ligands in various research [28, 29].

$$\Delta Gbind = \Delta Gcomplex - [\Delta Greceptor + \Delta Gligand]$$

Here, ΔG_{bind} denotes total free binding energy, while others denote the free energy of the protein, the ligand, and the complex. The following equation was used to calculate specific energy term contribution to the total free energy:

$$G = Gbond + Gele + GvdW + Gpol + Gnpol$$

Bonded, electrostatic, polar, non-polar, and Van der Waals energy terms are represented by the above equation.

Unsupervised Clustering of MD Trajectories

The internal and localized motions of each trajectory were clustered by using the principal component analysis (PCA) approach [30, 31]. For the clustering of each trajectory, a CPPTRAJ module was used to compute the positional covariance matrix for eigenvectors and their atomic coordinates. Orthogonal coordinate's transformation was used to diagonalize the matrix of eigenvalues. Finally, the PCs were acquired based on eigenvalues and eigenvectors, which clustered the motions of each trajectory during the 200 ns of simulation [32, 33].

Free Energy Landscape (FEL)

Conformational transition, i.e., stable and metastable states separated by a subspace, which demonstrates an intermediate state, was obtained from the two PCs by mapping the FEL using *g_sham* module of Gromacs. The two PCs, PC1 and PC2, were used to calculate the free energy landscape (FEL) in the following equation.

$$\Delta G(X) = -K_{\mathrm{B}} T ln P(X)$$

where X indicates the response of the two principal components, K_{B} is Boltzmann constant, and $P(X)$ is the dispersion of the framework's likelihood on the first two principal components.

Results and Discussion

Because of its essential role in viral replication and immune evasion, PLpro is a promising therapeutic target. Hence, here we perform structure-based virtual screening of the NPASS (natural product activity and species source database) of the SARS-CoV-2 PLpro to identify potential inhibitors from natural sources that could act as promising hits for the treatment of COVID-19. A co-crystallized complex of PLpro with GRL0617 inhibitor (*5-amino-2-methyl-N-[(1R)-1-naphthalen-1-ylethyl]benzamide*) was downloaded from the protein databank. Four different domains, i.e., palm, fingers, thumb, and Ubl, make a structure of PLpro with an active site at the interface of the palm and thumb region and comprise of Asp164, Tyr264, Tyr268, and Gln269. The 3D structure of PLpro with the domain organization and the binding of GRL0617 in the active site is given in Fig. 1A. A catalytic triad present in the palm region of the PLpro comprised of Cys111, His272, and Asp286 where the cysteine (Cys111) is replaced by serine in the mutant versions, i.e., Alpha, Beta, Delta, Omicron, and Deltacron (Fig. 1B). In the current study, the native co-crystallized drug GRL0617 was considered a control to compare the activity of the novel hits using molecular screening and simulation approaches. The 2D interaction pattern and structure of GRL0617 is given in Fig. 1C and D.

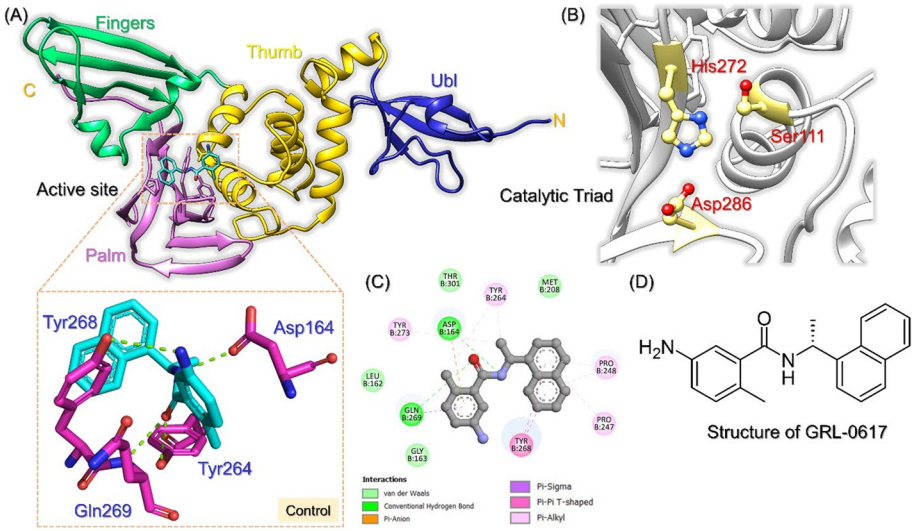

Fig. 1 Structural analysis of PLpro protein from SARS-CoV-2. **A** The domain organization of the PLpro protein where the four different domains, i.e., palm, fingers, thumb, and Ubl, are colored differently. **B** The catalytic triad present in the palm region of PLpro. **C** The 2D interaction pattern of the control drug GRL0617. **D** The 2D structure of the control drug (GRL0617)

Molecular Screening of NPASS

NPASS is a well-established natural products' (NPs) database, which is comprised of 35,032 NPs from 25,041 different sources (plants) tested against 5863 biological targets with 446,552 experimental assays. A large number of studies to discover novel drugs against different drug targets or repurpose the activity of these compounds use the database. Hence, considering the wider applicability and easy availability of the NPs, we also used NPASS to identify potential hits that could inhibit PLpro in the experimental assay and inhibit SARS-CoV-2. Before screening, the database was filtered for the compounds which obey the Lipinski's rule of five using FAFDrug4 which revealed that among the 35,032 compounds, 25,433 obey these rules while the rest 9599 were discarded. We performed the docking of the control drug to validate the docking protocol using AutoDock Vina, which revealed a docking score of −6.35 kcal/mol for GRL0617. In the next step, the screening of the 25,433 compounds was performed which revealed 35 compounds to have docking scores better than the control drug. The selection was also based on the interactions with the key essential residues that are functionally important. For the 25,433 compounds, the docking scores range from −7.05 to −4.28 kcal/mol. From these, the top scoring 35 compounds (docking scores range from −7.05 to −6.72 kcal/mol) were selected for IFD docking. Re-scoring of the top hits revealed that three compounds, i.e., NPC320891 (2,2-Dihydroxyindene-1,3-Dione), NPC474594 (Isonarciclasine), and NPC474595 (7-Deoxyisonarciclasine), exhibit higher docking scores than GRL0617.

Binding Mode of GRL0617 and NPC320891

Next, the binding mode of each of the top hits and GRL0617 was evaluated to reveal the interaction pattern with PLpro. As given in Fig. 1A and C, the GRL0617 mainly established four hydrogen bonds involving Asp164, Tyr264, Tyr268, and Gln269 residues. Along these residues,

Pro247 and Pro248 were observed to be involved in pie-pie and pie-alkyl interactions. The binding mode of NPC320891 demonstrated additional hydrogen bonds with a docking score − 7.03 kcal/mol. It is an organic compound and was originally discovered to detect ammonia. As given in Fig. 2A, the NPC320891 established five hydrogen bonds involving Asp164, Tyr264, Tyr273, and Gln269 residues. Residues Asp164, Tyr273, and Gln269 established a single hydrogen bond, while Tyr273 formed two hydrogen bonds. Moreover, a pie-pie and pie-alkyl interaction were also reported in this complex formed by Gly163 and Gln269. Thus, this shows the stronger binding of NPC320891 with the key active site residues of PLpro than GRL0617 to inhibit SARS-CoV-2. The 3D and 2D interaction patterns of NPC320891 are given in Fig. 2A and B.

Binding Mode of NPC474594

Interaction of NPC474594 with PLpro revealed that this compound established seven hydrogen bonds including Lys157, Asp164, Glu167, Tyr264, Tyr268, and Gln269. Interestingly with the new hydrogen bonding contacts, most of them are strongly conserved with the control drug; this shows the accuracy of the binding mode. This compound also established several pie-pie and pie-alkyl interactions with the key active site residues. The docking score for NPC474594 (Isonarciclasine) was reported to be − 6.99 kcal/mol. Hence, this shows that the establishment of essential extra interactions helps in robust binding and blocking of key residues of PLpro to inhibit the role of PLpro in COVID-19 progression. The interaction pattern of NPC474594 (Isonarciclasine) is given in Fig. 3A (3D) and B (2D).

Binding Mode of NPC474595

It shares a similar scaffold with NPC474594 (Isonarciclasine) except exclusion of oxygen from C7 and has been isolated from the same source. The interaction pattern of NPC474595 is strongly conserved as NPC474594 by establishing seven hydrogen bonds including Lys157, Asp164, Glu167, Tyr264, Tyr268, and Gln269. Moreover, the hydrophobic interactions are also strongly conserved between the NPC474594 and NPC474595. The docking score for NPC474595 and PLpro was reported to be − 6.93 kcal/mol, while

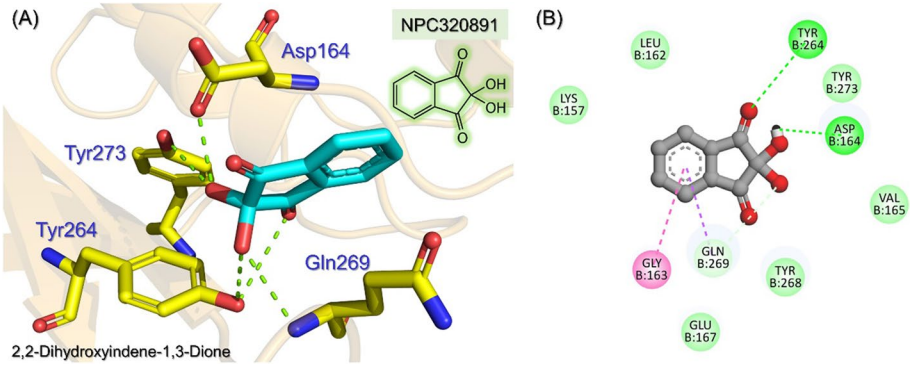

Fig. 2 Interaction pattern of NPC320891 (2,2-Dihydroxyindene-1,3-Dione) with PLpro. **A** The 3D interaction pattern where the green dotted lines represent hydrogen bonds, **B** the 2D interaction pattern of NPC32081. The green dotted lines represent hydrogen bonds while the purple and pink show pie-pie and pie-alkyl bonds

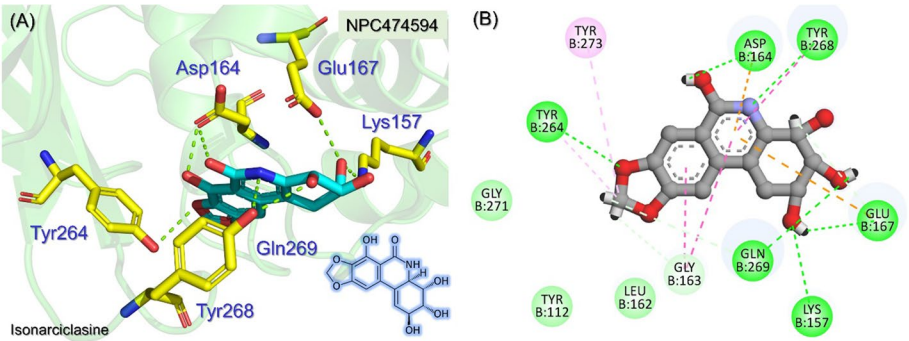

Fig. 3 Interaction pattern of NPC474594 (Isonarciclasine) with PLpro. **A** The 3D interaction pattern where the green dotted lines represent hydrogen bonds, **B** the 2D interaction pattern of NPC474594 (Isonarciclasine). The green dotted lines represent hydrogen bonds while the purple and pink show pie-pie and pie-alkyl bonds

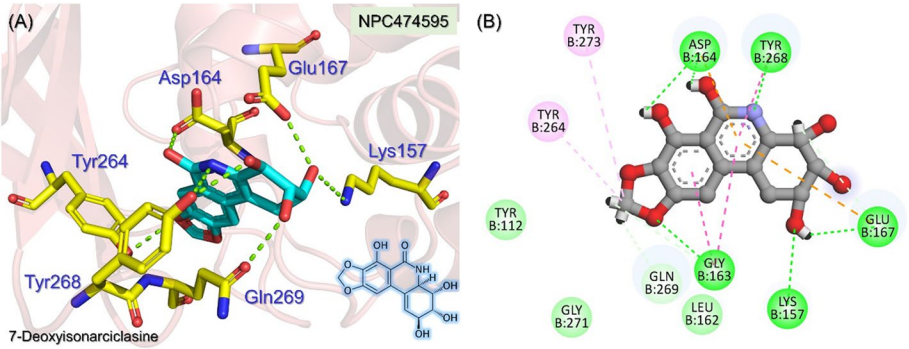

Fig. 4 Interaction pattern of NPC474595 (7-Deoxyisonarciclasine) with PLpro. **A** The 3D interaction pattern where the green dotted lines represent hydrogen bonds, **B** the 2D interaction pattern of NPC474595 (7-Deoxyisonarciclasine). The green dotted lines represent hydrogen bonds while the purple and pink show pie-pie and pie-alkyl bonds

Table 1 The docking scores of the control and top three hits

S. No	Compound name	Docking score (kcal/mol)
1	GRL0617 (control)	−6.35
2	NPC320891 (2,2-dihydroxyindene-1,3-dione)	−7.03
3	NPC474594 (isonarciclasine)	−6.99
4	NPC474595 (7-deoxyisonarciclasine)	−6.93

the interaction modes are given in Fig. 4A (3D) and B (2D). In sum, these three hits exhibit stronger inhibitory features in contrast to the native ligand as these hits target the essential residues and alter the activity of PLpro. The docking score of the control and top three hits

are shown in Table 1. To further validate the binding and inhibitory potential, these top three compounds were subjected to molecular simulation for further validation.

Dynamic Stability Assessment of the PLpro-Ligand Complexes

Determination of structural and binding stability in a dynamic environment is an essential assessment to understand the inhibitory features of a particular drug or small molecule. It has been a key assessment to see the impact of the binding of small molecules, the interaction of two proteins, and the impact of the mutation on the protein structure and function. Hence, to compute the dynamic stability of each complex, we calculated RMSD (root mean square deviation) using the simulation time and trajectories. As given in Fig. 5a, the control drug (GRL0617) in complex with PLpro demonstrated comparatively unstable dynamic behavior than the three hits. The RMSD started from 0 Å and increased up to 1.5 Å during the first 5 ns and then started gradually increased until 60 ns. Afterward, the RMSD gradually increased but significant deviations were observed between 61 and 115 ns. Then, the trajectory started decreasing the RMSD until 135 ns and then again with significant deviations continued until 200 ns. This increase and decrease in the RMSD graph demonstrate the destabilized dynamics of the PLpro-GRL0617 complex. An average RMSD for this complex was calculated to be 2.35 Å. On the other hand, the PLpro-NPC320891 comparatively demonstrated a very stable dynamic behavior than the control drug. The structure initially reported deviations between 1 and 25 ns and then continues to follow a uniform pattern until 45 ns. The RMSD increased afterward and then a stable uniform stability pattern was reported until 165 ns. After 165 ns, the RMSD decreased back and remained consistent until the end of the simulation. An average RMSD was reported to be 2.80 Å. This shows that despite the higher RMSD value, the PLpro-NPC320891 remained more stable than the control drug (GRL0617). The RMSD graph of the PLpro-NPC320891 is given in Fig. 5a. In the case of NPC474594-PLpro complex, a very stable dynamic behavior was observed. No significant deviation was observed during the simulation time. This complex just reported minor deviations at 60 ns and 84 ns and then a uniform straight RMSD until

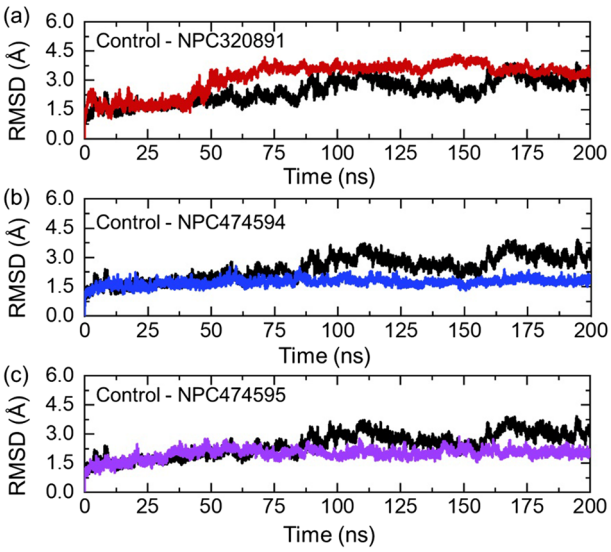

Fig. 5 Stability analysis of the control drug and the top three hits in complex with PLpro from SARS-CoV-2. **a** The RMSD for GRL0617-PLpro and NPC320891-PLpro. **b** The RMSD for GRL0617-PLpro and NPC474594-PLpro. **c** The RMSD for GRL0617-PLpro and NPC474595-PLpro

the end of the simulation was observed. An average RMSD for the NPC474594-PLpro complex was calculated to be 1.5 Å. Similarly, the NPC474595-PLpro demonstrated a similar pattern as NPC474594. The RMSD continues to increase a little during 1–65 ns and then decreased back. No significant deviations were observed except minor deviations at 84 ns, 114 ns, and 165 ns. An average RMSD for the NPC474595 was calculated to be 1.65 Å. Both the NPC474594 and NPC474595 complexes reported more stable dynamic behavior than the control drug and NPC320891. The RMSD graphs for NPC474594 and NPC474595 are given in Fig. 5b and c. In all the complexes, the RMSD converged with the control during the first 50 ns; this implies that the complexes had already reached the required equilibrium and stability state. Hence, it shows that the identified three hits possess stable dynamic behavior, which consequently reflects the stable binding of these molecules and the determination of excellent inhibitory properties to the control drug. To further understand how the binding of these drugs affects the conformation of PLpro, we retrieved different snapshots at different time intervals from the simulation trajectories. For the control drug, complex structures at 13 ns, 60 ns, 88 ns, 115 ns, and 158 ns were retrieved and compared with the native structure. In the case of NPC320891, structures at 12 ns, 18 ns, 50 ns, and 164 ns and a single structure at 84 ns were retrieved from the trajectory of NPC474594. On the other hand, structures at 84 ns, 114 ns, and 165 ns were retrieved from the NPC474595 trajectory. In most of the case, it was observed that the loop in the fingers and the loop harboring the catalytic triad move inward and outward which increases the volume as the loops open up while forming a closed cavity when moving inward which consequently releases and holds the ligand inside the cavity. In the case of NPC4745954-PLpro and NPC474595-PLpro complexes, in and out movements are stabilized by the extra interactions, which consequently results in stable dynamics.

Dynamics-Based Compactness Analysis of the Top Scoring Compounds

During molecular simulation, structural compactness provides vital information about binding and unbinding events. This essential calculation provides information regarding the size of the protein calculated as the radius of gyration (Rg) using the simulation

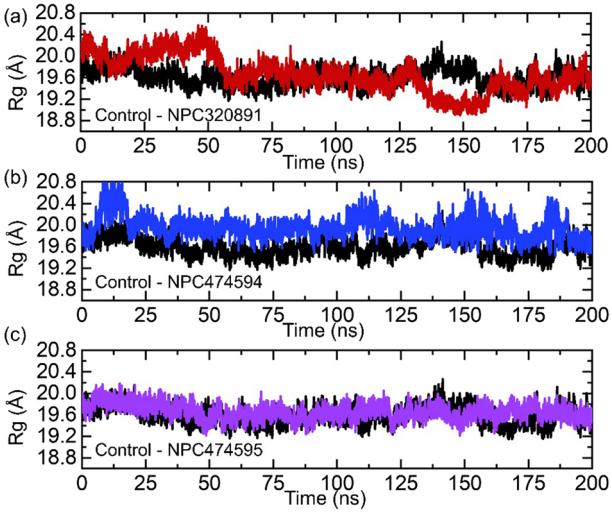

Fig. 6 Structural compactness analysis of the control drug and the top three hits in complex with PLpro from SARS-CoV-2. **a** The Rg for GRL0617-PLpro and NPC320891-PLpro. **b** The Rg for GRL0617-PLpro and NPC474594-PLpro. **c** The Rg for GRL0617-PLpro and NPC474595-PLpro

trajectories. Herein, alike results were observed as the RMSD for each complex. As given in Fig. 6a, the Rg of the control complex started at 20.0 Å and continues to gradually decrease reaching to 19.2 Å at 50 ns. Afterward, the Rg of the control stabilized at 19.2 Å until 85 ns and then continues to increase gradually till 110 ns, and then an abrupt decline for a shorter period was observed. Furthermore, the Rg remained higher between 115 and 155 ns and then finally stabilized at the end of the simulation. The same trend was observed in the RMSD where a stabilized pattern was reported in the terminal simulation. The continuous increase and decrease in the Rg over the different time intervals demonstrate significant binding and unbinding events that occurred during simulation, which increase and decrease the size of the protein. On the other hand, as shown in Fig. 6a, the NPC320891-PLpro during the first 0–50 ns demonstrated a higher Rg than the control but then a hasty decline was observed in the Rg after 50 ns. The Rg then stably continues until 138 ns, and then again, an abrupt decline in the Rg was observed and continues between 139 and 160 ns. The Rg can be seen increased in the later part of the simulation. Hence, this informs that the complex remained more compact during the simulation withstanding the stable interactions and minimizing the unbinding events during the simulation. Moreover, for the NPC474594-PLpro complex, the Rg between 3 and 8 ns demonstrated higher Rg and then a uniform Rg value throughout the simulation was observed except between 100–125 ns and 150–160 ns where minor deviation in the Rg was experienced by the complex. Overall, the complex demonstrated a tight packing of the protein as compared to the control and NPC320891-PLpro complexes. The Rg graph for the NPC474594-PLpro complex is given in Fig. 6b. Furthermore, consistent with the RMSD, the NPC474595-PLpro complex reported a uniform Rg pattern throughout the simulation (Fig. 6c). Starting from 19.80 Å from the start of the simulation, a gradual decrease was observed until 50 ns. Afterward, the Rg graph remained consistent with no significant deviations experienced by the complex during the simulation. In conclusion, the overall results demonstrate a tight packing of the NPC320891-PLpro. NPC4745954-PLpro and NPC474595-PLpro complexes than GRL0617-PLpro, which resultantly report the trapping of these small molecules in the binding cavity. Thus, show comparatively strongly activity against PLpro than the GRL0617 inhibitor.

Residual Flexibility Assessment of Top Scoring Compounds and NRP1 Complexes

Estimating the flexibility index of each amino acid during simulation is critical for understanding its involvement in binding, recognition, catalysis, inhibition, and conformational changes. To understand the flexibility of each complex upon the binding of ligand, we computed root mean square fluctuation (RMSF) and presented it in Fig. 7a–c. As given in Fig. 7a, all the complexes demonstrated a more similar pattern of flexibility in the region 1–119 with no significant flexibility; however, the regions 120–140, 160–180, and 205–215. The 120–140 and 160–180 lie in the fingers' region of PLpro, which may open/close during the simulation to cover the active site and push the ligand inside. The flexibility of 120–140 and 160–180 regions are given in Fig. 7b. On the other hand, the region 205–215 lies in the palm domain, which also harbor the catalytic triad, reported higher flexibility for the control and NPC320891-PLpro complexes (Fig. 7c). These findings are consistent with the RMSD as both of these demonstrated similar RMSD patterns. The other two complexes demonstrated small fluctuations for the region 205–215 which consequently show that these two ligands result in stabilization of residual flexibility, which

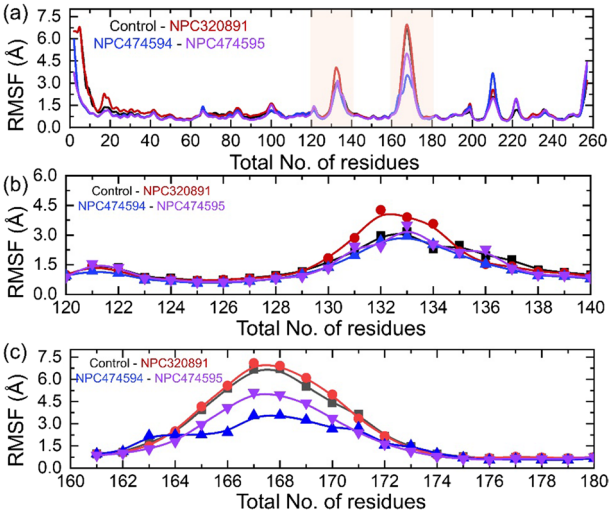

Fig. 7 RMSF graphs of GRL0617-PLpro, NPC320891-PLpro, NPC474594-PLpro, and NPC474595-PLpro complexes. **a** Whole protein RMSF for all the complexes, **b** RMSF of region 120–140, while **c** represents RMSF of 160–180 region

consequently produces minimal fluctuations. Hence, this shows that the two drugs comparatively produced stronger binding effects than the control and NPC320891.

Hydrogen Bonding Analysis

Quantification of hydrogen bonding between the interacting molecules reveals important information about the inhibitory features of the interacting drugs. Hydrogen bonds are among the key elements that define the inhibitory effects of the binding drug. An increase and decrease in the number of hydrogen bonds consequently alter the binding affinity of the interacting molecule. It has been previously used to estimate the hydrogen-bonding paradigm to report how the new variants of SARS-CoV-2 differentially affect the binding with the hACE2 by altering the hydrogen-bonding paradigm. Moreover, it has also been used in discovering novel drugs against the receptor-binding domain (RBD) of the Omicron variant. Firstly, we calculated an average number of hydrogen bonds in each trajectory to see how the bonding is affected throughout the simulation time. As given in Fig. 8a–d, the average number of hydrogen bonds in the control was calculated to be 118; in NPC320891-PLpro, the average number of hydrogen bonds was computed to be 120; and in the NPC474594-PLpro complex, the average number of hydrogen bonds was 125, while in the NPC474595-PLpro complex, the number of hydrogen bonds was reported to be 122. Hence, this shows that the two drugs particularly (NPC474594 and NPC474595) exhibit a stronger affinity for the active site of PLpro and thus produce better inhibitory effects in contrast to the control drug.

To calculate the hydrogen bond half-life during the simulation, the whole simulation trajectories were subjected to hydrogen bonding analysis. We considered only essential residues such as Lys157, Asp164, Glu167, Tyr264, Tyr268, and Gln269 for hydrogen bonding half-life during the simulation. In only two complexes, i.e., NPC474594-PLpro and NPC474595-PLpro, the Lys157 bond was detected in 64% and 57% of the total trajectories. The Asp164 interaction sustained in 73% trajectory in GRL0617-PLpro, 69% in NPC320891-Plpro, 81% in NPC474594-PLpro, and 78% in NPC474595-PLpro complex.

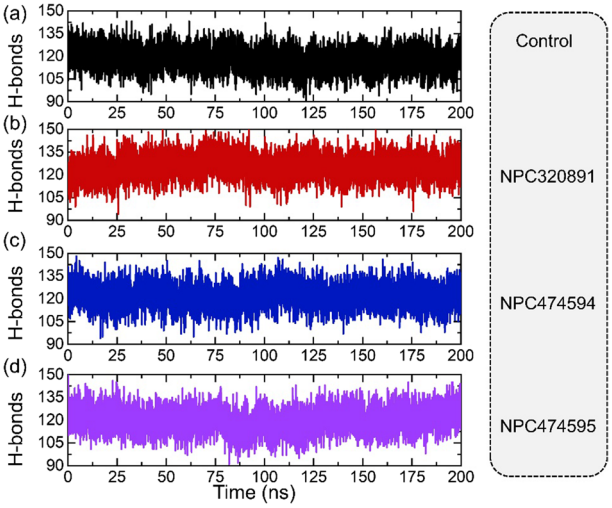

Fig. 8 Hydrogen bonding analysis of GRL0617-PLpro, NPC320891-PLpro, NPC474594-PLpro and NPC474595-PLpro complexes. **a** Hydrogen bonding graph for of GRL0617-PLpro complex, **b** hydrogen bonding graph for NPC320891-PLpro complex, **c** hydrogen bonding graph for NPC474594-PLpro complex, while **d** hydrogen bonding graph for NPC474595-PLpro complex

On the other hand, the Glu167interaction sustained in 21% in GRL0617-PLpro, 27% in NPC320891-PLpro, 65% in NPC474594-PLpro, and 68% in NPC474595-PLpro complex. Moreover, the Tyr264 interaction sustained in 44% in the GRL0617-PLpro complex, 47% in NPC320891-PLpro, 52% in NPC474594-PLpro, and 45% in the NPC474595-PLpro complex. Furthermore, Tyr268 interaction sustained in 03% trajectory only in GRL0617-PLpro, 41% in NPC474594-PLpro, 34% in NPC474595-PLpro, while not detected in NPC320891-PLpro complex. Finally, the Gln269 interaction was reported in 63% of the GRL0617-PLpro trajectory, 69% in NPC320891-PLpro, 74% in NPC474594-PLpro, and 71% of NPC474595-PLpro trajectory. Thus, this shows that mostly the bonding remained conserved; however, the extra interactions with the other active site residues by the three hits make them more favorable than the control drug. The hydrogen bonding fraction analysis is given in Table 2.

Table 2 The hydrogen bonding fraction analysis results of GRL0617-PLpro, NPC320891-PLpro, NPC474594-PLpro, and NPC474595-PLpro complexes

Residues	GRL0617-PLpro	NPC320891-PLpro	NPC474594-PLpro	NPC474595-PLpro
Lys157	-	-	64%	57%
Asp164	73%	69%	81%	78%
Glu167	21%	27%	65%	68%
Tyr264	44%	47%	52%	45%
Tyr268	03%	-	41%	34%
Gln269	63%	69%	74%	71%

Table 3 The binding free energy calculation results from molecular simulation using MM/GBSA analysis. All the results are calculated in kcal/mol

Parameters	GRL0617-PLpro	NPC320891-PLpro	NPC474594-PLpro	NPC474595-PLpro
vdW	−37.45 ± 0.18	−38.64 ± 0.20	−44.37 ± 0.18	−42.41 ± 0.17
EEL	−7.68 ± 0.18	−8.41 ± 0.19	−10.54 ± 0.18	−9.33 ± 0.14
EGB	15.79 ± 0.15	15.78 ± 0.17	17.66 ± 0.17	16.11 ± 0.15
ESURF	−3.31 ± 0.01	−4.31 ± 0.02	−6.47 ± 0.02	−5.98 ± 0.02
Delta G Gas	−45.13 ± 0.23	−54.22 ± 0.28	−72.48 ± 1.34	−64.15 ± 1.02
Delta G Solv	12.48 ± 0.15	19.52 ± 0.17	18.09 ± 1.01	18.24 ± 0.93
Delta total	**−32.65 ± 0.17**	**−35.58 ± 0.14**	**−43.72 ± 0.22**	**−41.61 ± 0.20**

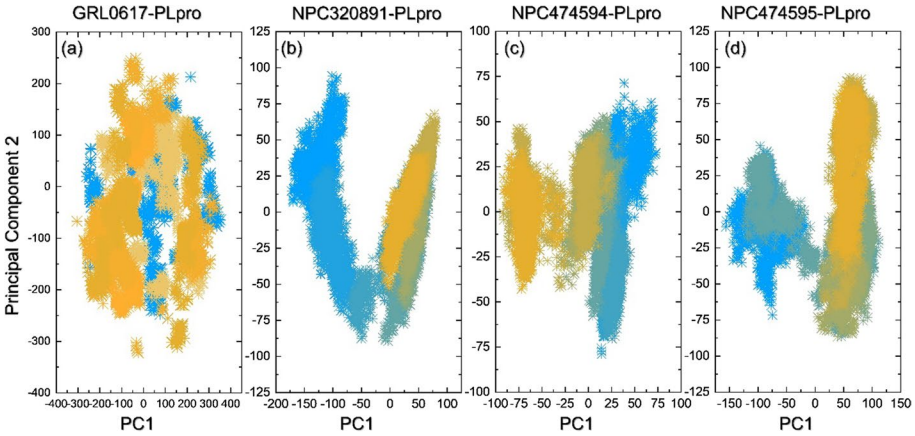

Fig. 9 Principal component analysis (PCA) of GRL0617-PLpro, NPC320891-PLpro, NPC474594-PLpro and NPC474595-PLpro complexes. **a** PCA of GRL0617-PLpro complex, **b** PCA of NPC320891-PLpro complex, **c** PCA of NPC474594-PLpro complex, and **d** represent PCA of NPC474595-PLpro complex

Binding Free Energy Calculation

Re-evaluation of the accurate binding conformation and energy can be computed with the Gibbs binding free energy method. This approach is predominantly the most frequently employed and accurate for re-ranking the most potent inhibitor against the respective receptor. It is computationally inexpensive and had the advantage over other rational methods. Hence, considering the accuracy and applicability, we estimated the binding free energy using MM/GBSA approach. The vdW energy for GRL0617-PLpro was calculated to be −37.45 ± 0.18 kcal/mol and −38.64 ± 0.20 kcal/mol for NPC320891-Plpro; for NPC474594-PLpro, the vdW was −44.37 ± 0.18 kcal/mol, while the NPC474595-PLpro demonstrated a vdW of −42.41 ± 0.17 kcal/mol, respectively. Finally, the total binding free energy was reported to be −32.65 ± 0.17 kcal/mol for the GRL0617-PLpro; for the NPC320891-PLpro complex, the TBE was −35.58 ± 0.14 kcal/mol; for the NPC474594-PLpro, the TBE was −43.72 ± 0.22 kcal/mol, while for NPC474595-PLpro complex, the TBE was calculated to be −41.61 ± 0.20 kcal/mol, respectively. It can be seen that the TBE

of all the complexes is higher than the control drug GRL0617 that consequently shows that the three hits could inhibit the PLpro more strongly and need further in vivo and in vitro validation for the possible usage as a potential drug against SARS-CoV-2. The binding free energy results are shown in Table 3.

Principal Component Analysis (PCA)

For clustering, similar conformation structures in the simulation trajectories PCA analysis was performed for each complex. As given in Fig. 9a–d, the control drug demonstrated different dynamic motions than the three hits. The control drug reported 56% motion by the first three eigenvectors, while the three hits, i.e., NPC320891-PLpro, NPC474594-PLpro, and NPC474595-PLpro demonstrated 51%, 48%, and 46% of the total internal motion by the first three eigenvectors. These results strongly corroborate with the RMSF results where lower fluctuation was observed for the novel three hits. Given in the figure, the two colors sky blue and orange represent the two conformations, while the transition states are represented by the light grey and yellow color. In sum, this shows that the identified three hits demonstrate different internal motions, thus showing a different approach for the interaction and inhibition of PLpro.

Free Energy Landscape (FEL)

Next, we mapped these PCs to construct the free energy landscape where the metastable state can be easily identified. The constructed FEL maps for all the complexes are given in Fig. 10a–d. All the complexes attained one lowest energy conformational state which is given in Fig. 10a–d represented by the black circle. In the case of the wild type, the lowest energy conformation state was attained at 103 ns where the conformational changes were also identified. The terminal loop and the opening up of the fingers region were identified

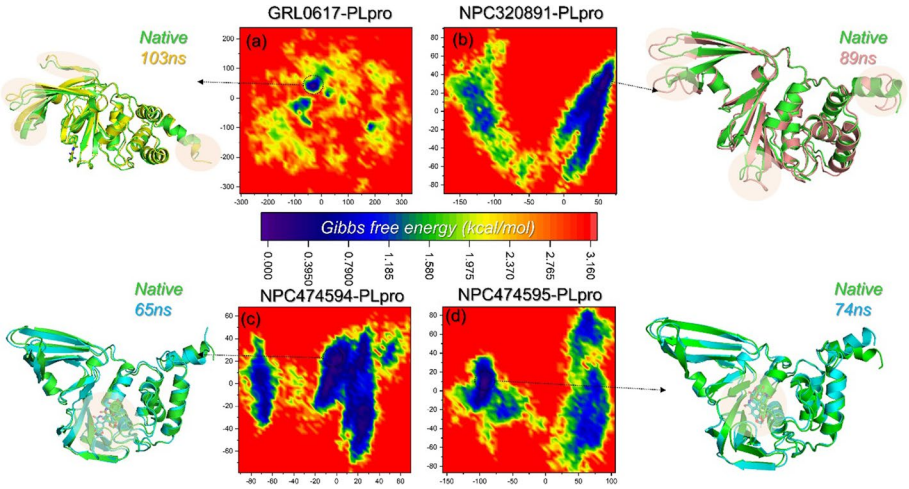

Fig. 10 Free energy landscape of GRL0617-PLpro, NPC320891-PLpro, NPC474594-PLpro, and NPC474595-PLpro complexes. **a** FEL of GRL0617-PLpro complex, **b** FEL of NPC320891-PLpro complex, **c** FEL of NPC474594-PLpro complex, while **d** represents FEL of NPC474595-PLpro complex

which shows that due to opening of the fingers region and the palm loop provides more volume for the drug. On the other hand, the NPC320891-PLpro complex attained the lowest energy state at 89 ns where along side the similar structural changes i.e. conversion of the helix into a loop was also observed. Moreover, the two complexes, i.e., NPC474594-PLpro complex and NPC474595-PLpro complex, attained the lowest energy conformations at 65 ns and 74 ns, respectively. In both the complexes, the structures remained strongly conserved as the native structure however; the drug was seen to have moved inside the binding cavity along with the loop in the palm region harboring the catalytic triad, thus justifying the higher binding of these two molecules particularly. Hence, the overall results reflect the conformation and dynamic changes that favor the binding of the identified hits more favorably than the control drug.

Discussion

The COVID-19 outbreak has posed serious socioeconomic problems for humanity. The COVID-19 pandemic was not properly controlled by the already authorized antivirals, and we are just now discovering how important it is to develop new antiviral treatments in advance to control the potential outbreaks of this and other zoonotic viruses. One key step in ending the epidemic was faster approval and distribution of the first vaccines. However, there are concerns about the protracted consequences of COVID-19 immune protection in a population with highly diverse seroprevalence in Manaus, Brazil, as well as compelling research that those who have been infected with the Alpha, Beta, and Gamma variants are more vulnerable to the highly infectious Delta variant. Antiviral agents that complement vaccination are urgently needed to end the COVID-19 pandemic. The SARS-CoV-2 proteome is comprised of essential proteins; however, PLpro is one of the two essential cysteine proteases, which helps the virus to regulate the process of replication and dysregulates the host immune sensing upon the interaction and deubiquitination of host protein substrates. It also processes the viral polyproteins, targets the host interferon, and NF-κB pathways, and generates a functional replicase complex. Natural products are the freely available medicinal flora for the treatment of various diseases [34–37].

We shortlisted three compounds as potential inhibitors of PLpro from SARS-CoV-2 which include NPC320891 (2,2-Dihydroxyindene-1,3-Dione), NPC474594 (Isonarciclasine), and NPC474595 (7-Deoxyisonarciclasine). In comparison with the control drug, GRL0617, our shortlisted compounds exhibit higher docking scores. As Asp164, Tyr264, Tyr268, and Gln269 residues are essential for the interaction and inhibition of PLpro, the shortlisted compounds alongside these residues also established Gly163 and Gln269 pie-pie and pie-alkyl interactions with the active site. These interactions are also reported by a previously published study on PLpro-GRL0617 co-complex, thus validating the accuracy of our docking and results [38]. More importantly, the interaction with Glu167 established a hydrogen bond, which has been previously, reported that target this residue and mimic the ubiquitination that consequently inhibits the PLpro [19, 39]. NPC474594 (Isonarciclasine) was originally isolated from Amaryllidaceae isoquinoline with the reported antiviral activity against the RNA viruses including Japanese encephalitis, yellow fever, dengue viruses, Punta Toro, sandfly fever, Rift Valley fever viruses, Venezuelan equine encephalomyelitis virus, lentivirus human immunodeficiency virus type 1, and the DNA-containing vaccinia virus [40]. The antiviral activity of NPC474595 or 7-Deoxyisonarciclasine has

also been reported against Japanese encephalitis, yellow fever, dengue viruses, Punta Toro, sand fly fever, Rift Valley fever viruses, Venezuelan equine encephalomyelitis virus, lentivirus human immunodeficiency virus type 1, and the DNA-containing vaccinia virus [39, 40]. The shortlisted compounds mostly block the loop residues which are reported to have an essential role in the pathological implications of the interaction with ISG15 [41].

Moreover, the structural dynamics properties of each complex including RMSD, RMSF, Rg, hydrogen bonding, binding free energy calculation, PCA, and FEL also revealed favorable features as compared to the control drug. In each complex, the structures remained strongly conserved as the native structure however; the drug was seen to have moved inside the binding cavity along with the loop in the palm region harboring the catalytic triad, thus justifying the higher binding of these two molecules particularly. Hence, the overall results reflect the conformation and dynamic changes that favor the binding of the identified hits more favorably than the control drug. The current study may suffer from the emerging challenging variants that may evade the anti-viral effects of these shortlisted compounds. Moreover, in vitro validation of these compounds remains a limitation of the current study.

Conclusions

Because of the essential role of PLpro in the regulation of replication and dysregulation of the host immune sensing, we used a structure-based drug designing approach to identify potential small molecular inhibitors for PLpro of SARS-CoV-2. We identified three compounds NPC320891 (2,2-Dihydroxyindene-1,3-Dione), NPC474594 (Isonarciclasine), and NPC474595 (7-Deoxyisonarciclasine) which exhibit higher docking scores than the control GRL0617. With molecular simulation, we reported that 120–140 and 160–180 lie in the finger's region of PLpro, which may open/close during the simulation to cover the active site and push the ligand inside. In conclusion, the overall results reflect favorable binding of the identified hits strongly than the control drug thus demand in vitro and in vivo validation for clinical purposes. In conclusion, this study provides a basis for the development of novel drugs against SARS-CoV-2.

Acknowledgements The computations were partially performed at the PengCheng Lab. and the Center for High-Performance Computing, Shanghai Jiao Tong University.

Author Contribution All the authors were involved in designing, analyzing, writing, and revising the manuscript.

Funding We thank the Ministry of Higher Education Malaysia (MoHE), fundamental research grant scheme (FRGS/1/2021/STG04/USM/02/14) for supporting this research.

Data Availability All the data is available on RCSB and UniProt and any simulation data would be provided on reasonable demand. The accession numbers to access this data are given in the manuscript.

Declarations

Ethical Approval Not applicable.

Consent to Participate Not applicable.

Consent for Publication Not applicable.

Competing Interests The authors declare no competing interests.

References

1. Tao, K., Tzou, P. L., Nouhin, J., Gupta, R. K., de Oliveira, T., Kosakovsky Pond, S. L., Fera, D., & Shafer, R. W. (2021). The biological and clinical significance of emerging SARS-CoV-2 variants. *Nature Reviews Genetics, 22*(12), 757–773.
2. Velavan, T. P., & Meyer, C. G. (2020). The COVID-19 epidemic. *Tropical medicine & international health, 25*(3), 278.
3. Zhu, N., Zhang, D., Wang, W., Li, X., Yang, B., Song, J., Zhao, X., Huang, B., Shi, W., & Lu, R. (2020). A novel coronavirus from patients with pneumonia in China, 2019. *New England journal of medicine, 382*(8), 727.
4. Tortorici, M. A., & David V. (2019) *Structural insights into coronavirus entry. Advances in virus research* (vol. 105, pp. 93-116). Academic Press.
5. Wrapp, D., Wang, N., Corbett, K. S., Goldsmith, J. A., Hsieh, C.-L., Abiona, O., Graham, B. S., & McLellan, J. S. (2020). Cryo-EM structure of the 2019-nCoV spike in the prefusion conformation. *Science, 367*(6483), 1260–1263.
6. Burkard, C., Verheije, M. H., Wicht, O., van Kasteren, S. I., van Kuppeveld, F. J., Haagmans, B. L., Pelkmans, L., Rottier, P. J., Bosch, B. J., & de Haan, C. A. (2014). Coronavirus cell entry occurs through the endo-/lysosomal pathway in a proteolysis-dependent manner. *PLoS pathogens, 10*(11), e1004502.
7. Barretto, N., Jukneliene, D., Ratia, K., Chen, Z., Mesecar, A. D., & Baker, S. C. (2005). The papain-like protease of severe acute respiratory syndrome coronavirus has deubiquitinating activity. *Journal of virology, 79*(24), 15189–15198.
8. Fehr, A. R., Athmer, J., Channappanavar, R., Phillips, J. M., Meyerholz, D. K., & Perlman, S. (2015). The nsp3 macrodomain promotes virulence in mice with coronavirus-induced encephalitis. *Journal of virology, 89*(3), 1523–1536.
9. Setti, L., Passarini, F., De Gennaro, G., Barbieri, P., Perrone, M. G., Borelli, M., Palmisani, J., Di Gilio, A., Torboli, V., & Fontana, F. (2020). SARS-Cov-2RNA found on particulate matter of Bergamo in Northern Italy: First evidence. *Environmental research, 188*, 109754.
10. Petushkova, A. I., & Zamyatnin, A. A. (2020). Papain-like proteases as coronaviral drug targets: Current inhibitors, opportunities, and limitations. *Pharmaceuticals, 13*(10), 277.
11. Creech, C. B., Walker, S. C., & Samuels, R. J. (2021). SARS-CoV-2 vaccines. *JAMA, 325*(13), 1318–1320.
12. Chakravarti, R., Singh, R., Ghosh, A., Dey, D., Sharma, P., Velayutham, R., Roy, S., & Ghosh, D. (2021). A review on potential of natural products in the management of COVID-19. *RSC Advances, 11*(27), 16711–16735. https://doi.org/10.1039/D1RA00644D
13. Singla, R. K., He, X., Chopra, H., Tsagkaris, C., Shen, L., Kamal, M. A., & Shen, B. (2021). Natural products for the prevention and control of the COVID-19 pandemic: Sustainable bioresources. *Frontiers in Pharmacology, 12*, 758159. https://doi.org/10.3389/fphar.2021.758159
14. Khan, A., Heng, W., Wang, Y., Qiu, J., Wei, X., Peng, S., Saleem, S., Khan, M., Ali, S. S., & Wei, D.-Q. (2021). In silico and in vitro evaluation of kaempferol as a potential inhibitor of the SARS-CoV-2 main protease (3CLpro). *Phytotherapy Research, 35*(6), 2841–2845. https://doi.org/10.1002/ptr.6998
15. Fu, Z., Huang, B., Tang, J., Liu, S., Liu, M., Ye, Y., Liu, Z., Xiong, Y., Zhu, W., & Cao, D. (2021). The complex structure of GRL0617 and SARS-CoV-2 PLpro reveals a hot spot for antiviral drug discovery. *Nature communications, 12*(1), 1–12.
16. Mahmoudvand, S., & Shokri, S. (2021). Interactions between SARS coronavirus 2 papain-like protease and immune system: A potential drug target for the treatment of COVID-19. *Scandinavian journal of immunology, 94*(4), e13044.
17. Calleja, D. J., Lessene, G., & Komander, D. (2022). Inhibitors of SARS-CoV-2 PLpro. *Frontiers in Chemistry, 10*, 876212. https://doi.org/10.3389/fchem.2022.876212
18. Heo, L., Park, H., & Seok, C. (2013). GalaxyRefine: Protein structure refinement driven by side-chain repacking. *Nucleic acids research, 41*(W1), W384–W388.
19. Shen, Z., Ratia, K., Cooper, L., Kong, D., Lee, H., Kwon, Y., Li, Y., Alqarni, S., Huang, F., Dubrovskyi, O., Rong, L., Thatcher, G. R. J., & Xiong, R. (2022). Design of SARS-CoV-2 PLpro inhibitors for COVID-19 antiviral therapy leveraging binding cooperativity. *Journal of Medicinal Chemistry, 65*(4), 2940–2955. https://doi.org/10.1021/acs.jmedchem.1c01307
20. Ravindranath, P. A., Forli, S., Goodsell, D. S., Olson, A. J., & Sanner, M. F. (2015). AutoDockFR: Advances in protein-ligand docking with explicitly specified binding site flexibility. *PLOS Computational Biology, 11*(12), e1004586. https://doi.org/10.1371/journal.pcbi.1004586

21. Case, D. A., Cheatham, T. E., III., Darden, T., Gohlke, H., Luo, R., Merz, K. M., Jr., Onufriev, A., Simmerling, C., Wang, B., & Woods, R. J. (2005). The Amber biomolecular simulation programs. *Journal of computational chemistry, 26*(16), 1668–1688.
22. Price, D. J., & Brooks, C. L., III. (2004). A modified TIP3P water potential for simulation with Ewald summation. *The Journal of chemical physics, 121*(20), 10096–10103.
23. Roe, D. R., & Cheatham, T. E., III. (2013). PTRAJ and CPPTRAJ: Software for processing and analysis of molecular dynamics trajectory data. *Journal of chemical theory and computation, 9*(7), 3084–3095. https://doi.org/10.1021/ct400341p
24. Sun, H., Li, Y., Tian, S., Xu, L., & Hou, T. (2014). Assessing the performance of MM/PBSA and MM/GBSA methods. 4. Accuracies of MM/PBSA and MM/GBSA methodologies evaluated by various simulation protocols using PDBbind data set. *Physical Chemistry Chemical Physics, 16*(31), 16719–16729.
25. Hou, T., Li, N., Li, Y., & Wang, W. (2012). Characterization of domain–peptide interaction interface: Prediction of SH3 domain-mediated protein–protein interaction network in yeast by generic structure-based models. *Journal of proteome research, 11*(5), 2982–2995.
26. Chen, F., Liu, H., Sun, H., Pan, P., Li, Y., Li, D., & Hou, T. (2016). Assessing the performance of the MM/PBSA and MM/GBSA methods. 6. Capability to predict protein–protein binding free energies and re-rank binding poses generated by protein–protein docking. *Physical Chemistry Chemical Physics, 18*(32), 22129–22139.
27. Miller, B. R., III., McGee, T. D., Jr., Swails, J. M., Homeyer, N., Gohlke, H., & Roitberg, A. E. (2012). MMPBSA. py: An efficient program for end-state free energy calculations. *Journal of chemical theory and computation, 8*(9), 3314–3321.
28. Wang, Y., Khan, A., Chandra Kaushik, A., Junaid, M., Zhang, X., & Wei, D.-Q. (2019). The systematic modeling studies and free energy calculations of the phenazine compounds as anti-tuberculosis agents. *Journal of Biomolecular Structure and Dynamics, 37*(15), 4051–4069.
29. Khan, A., Kaushik, A. C., Ali, S. S., Ahmad, N., & Wei, D.-Q. (2019). Deep-learning-based target screening and similarity search for the predicted inhibitors of the pathways in Parkinson's disease. *RSC advances, 9*(18), 10326–10339.
30. Wold, S., Esbensen, K., & Geladi, P. (1987). Principal component analysis. *Chemometrics and intelligent laboratory systems, 2*(1–3), 37–52.
31. Pearson, K. (1901). LIII. On lines and planes of closest fit to systems of points in space. *The London, Edinburgh, and Dublin Philosophical Magazine and Journal of Science, 2*(11), 559–572.
32. Balsera, M. A., Wriggers, W., Oono, Y., & Schulten, K. (1996). Principal component analysis and long time protein dynamics. *The Journal of Physical Chemistry, 100*(7), 2567–2572.
33. Ernst, M., Sittel, F., & Stock, G. (2015). Contact-and distance-based principal component analysis of protein dynamics. *The Journal of chemical physics, 143*(24), 12B640_1.
34. de Oliveira Braz, A. V., Rodrigues, M. C., Maia, P. A. A., Pereira, A. P. D., de Lima, S. J., Santos, F. AVd., da Silva, L. E., Amaral, Wd., Santos, MLd., Coutinho, H. D. M., Baj, T., Kowalska, G., Kowalski, R., & Matias, E. F. F. (2022). GC-MS chemical characterization and antibacterial effect of the essential oil of Piper mosenii. *Molecules, 27*(18), 5911.
35. Pedroso de Lima, F., Lence, E., Suárez de Cepeda, P., Correia, C., Carvalho, M. A., González-Bello, C., & Proença, M. F. (2022). Regioselective synthesis of 2-aryl-5-cyano-1-(2-hydroxyaryl)-1H-imidazole-4-carboxamides self-assisted by a 2-hydroxyaryl group. *ACS Omega, 7*(27), 23289–23301. https://doi.org/10.1021/acsomega.2c01399
36. Manzoor, Y., Hasan, M., Zafar, A., Dilshad, M., Ahmed, M. M., Tariq, T., Hassan, S. G., Hassan, S. G., Shaheen, A., Caprioli, G., & Shu, X. (2022). Incubating green synthesized iron oxide nanorods for proteomics-derived motif exploration: A fusion to deep learning oncogenesis. *ACS Omega, 7*(51), 47996–48006. https://doi.org/10.1021/acsomega.2c05948
37. Zafar, A., Jabbar, M., Manzoor, Y., Gulzar, H., Hassan, S. G., Nazir, M. A., Ain Ul, H., Mustafa, G., Sahar, R., Masood, A., Iqbal, A., Hussain, M., & Hasan, M. (2020). Quantifying serum derived differential expressed and low molecular weight protein in breast cancer patients. *Protein and peptide letters, 27*(7), 658–673. https://doi.org/10.2174/0929866527666200110155609
38. Osipiuk, J., Azizi, S.-A., Dvorkin, S., Endres, M., Jedrzejczak, R., Jones, K. A., Kang, S., Kathayat, R. S., Kim, Y., Lisnyak, V. G., Maki, S. L., Nicolaescu, V., Taylor, C. A., Tesar, C., Zhang, Y.-A., Zhou, Z., Randall, G., Michalska, K., Snyder, S. A., … Joachimiak, A. (2021). Structure of papain-like protease from SARS-CoV-2 and its complexes with non-covalent inhibitors. *Nature Communications, 12*(1), 743. https://doi.org/10.1038/s41467-021-21060-3
39. Gabrielsen, B., Monath, T. P., Huggins, J. W., Kirsi, J. J., Hollingshead, M., Shannon, W. M., & Pettit, G. R. (1992). Activity of selected Amaryllidaceae constituents and related synthetic substances against medically important RNA viruses. *Natural products as antiviral agents*, 121–135.

40. Gabrielsen, B., Monath, T. P., Huggins, J. W., Kefauver, D. F., Pettit, G. R., Groszek, G., Hollingshead, M., Kirsi, J. J., Shannon, W. M., Schubert, E. M., et al. (1992). Antiviral (RNA) activity of selected Amaryllidaceae isoquinoline constituents and synthesis of related substances. *Journal of natural products, 55*(11), 1569–1581. https://doi.org/10.1021/np50089a003
41. Shin, D., Mukherjee, R., Grewe, D., Bojkova, D., Baek, K., Bhattacharya, A., Schulz, L., Widera, M., Mehdipour, A. R., Tascher, G., Geurink, P. P., Wilhelm, A., van der Heden van Noort, G. J., Ovaa, H., Müller, S., Knobeloch, K.-P., Rajalingam, K., Schulman, B. A., Cinatl, J., … Dikic, I. (2020). Papain-like protease regulates SARS-CoV-2 viral spread and innate immunity. *Nature, 587*(7835), 657–662. https://doi.org/10.1038/s41586-020-2601-5

Authors and Affiliations

Abrar Mohammad Sayaf[1] · Hassaan Ahmad[2] · Muhammad Ammar Aslam[2] · Sidra Abdul Ghani[3] · Saira Bano[3] · Qudsia Yousafi[4] · Muhammad Suleman[5] · Abbas Khan[6,7] · Kar Kheng Yeoh[1] · Dong-Qing Wei[6,7,8,9]

✉ Abbas Khan
biotechuos4@gmail.com

✉ Kar Kheng Yeoh
kkyeoh@usm.my

Hassaan Ahmad
hassanahmad6538@gmail.com

Muhammad Ammar Aslam
ammaeaslam901@gmail.com

[1] School of Chemical Sciences, Universiti Sains Malaysia, 11800 USM George Town, Penang, Malaysia

[2] Rawalpindi Medical University, Chamanzar Colony, Rawalpindi, Punjab 46000, Pakistan

[3] Department of Botany, University of Okara, Okara, Punjab, Pakistan

[4] Department of Biosciences, COMSATS University Islamabad-Sahiwal Campus, Sahiwal, Punjab, Pakistan

[5] Centre for Biotechnology and Microbiology, University of Swat, Swat, Khyber Pakhtunkhwa, Pakistan

[6] Department of Bioinformatics and Biological Statistics, School of Life Sciences and Biotechnology, Shanghai Jiao Tong University, Shanghai 200240, People's Republic of China

[7] Zhongjing Research and Industrialization, Institute of Chinese Medicine, Zhongguancun Scientific Park, Meixi, Nanyang, Henan 473006, People's Republic of China

[8] State Key Laboratory of Microbial Metabolism, Shanghai-Islamabad-Belgrade Joint Innovation Center On Antibacterial Resistances, Joint Laboratory of International Laboratory of Metabolic and Developmental Sciences, Ministry of Education and School of Life Sciences and Biotechnology, Shanghai Jiao Tong University, Shanghai 200030, People's Republic of China

[9] Peng Cheng Laboratory, Vanke Cloud City Phase I Building 8, Xili Street, Nanshan District, Shenzhen, Guangdong 518055, People's Republic of China